
Measurements of the Conduction Zone Length and Mass Ablation Rate in Cryogenic Direct-Drive Implosions on OMEGA

Electron thermal transport of energy through a plasma plays an important role in many areas of plasma physics.¹ In laser–matter experiments, the laser energy is absorbed near the critical surface and transported through the conduction zone by electrons to the ablation surface. This electron thermal transport governs the energy flow through the conduction zone, which determines the length of the conduction zone, the mass ablation rate, and ultimately the energy coupled to the target through the rocket effect. In inertial confinement fusion, where laser beams are used to drive a spherical capsule,² the mass ablation rate and the length of the conduction zone play a critical role in mitigating hydrodynamic instabilities that could limit the ultimate implosion performance.³ The conduction zone provides a buffer between the high-intensity modulations in the laser beam (speckles) and the ablation surface where these modulations seed the Rayleigh–Taylor (RT) instability,⁴ while the mass ablation reduces the growth of this instability by etching away the target material.^{2,5,6}

A complete description of electron thermal transport requires an understanding of both the laser–plasma interactions (e.g., inverse-bremsstrahlung, laser–plasma instabilities) and the conduction process. Laser–plasma interactions depend strongly on the plasma properties and the plasma properties depend on the laser–plasma interactions and the thermal transport, so a complete model must resolve both the laser wavelength scales and the kinetic motion of the plasma over large spatial scales. Historically, large hydrodynamic simulations have been limited to laser absorption by inverse-bremsstrahlung and Spitzer–Härm heat-transport models⁷ that use the local plasma conditions to calculate the laser absorption and heat flux. To account for the physics neglected in these simulations (e.g., laser–plasma instabilities, magnetic fields, and non-Maxwellian distribution functions), the flux was typically limited to a fraction of the free-streaming flux [$q_{fs} = n_e T_e (T_e/m_e)^{1/2}$, where n_e , T_e , and m_e are the electron density, temperature, and mass, respectively].⁸ Early experiments indicated that limiting the flux to 6% of the

free-streaming flux reproduced time-integrated observables,⁸ but to replicate the target trajectories, a time-dependent flux limiter was required.^{9–11}

To more accurately calculate the heat flux, nonlocal thermal-transport models have been developed.^{12–15} These models account for high-energy electrons that deposit their energy over a large distance, which tends to increase the mass ablation rate and the size of the conduction zone, but direct measurements of these effects are limited. Nonlocal thermal-transport models were required to accurately calculate the heat-wave propagation in relatively simple single-beam gas–target experiments¹⁶ and to simultaneously reproduce the shock timing and perturbation growth in more-sophisticated planar-target experiments.^{15,17} Recent implosion experiments have shown that nonlocal thermal transport¹⁵ and cross-beam energy transfer (CBET) models¹⁸ must be used to reproduce the coronal plasma conditions and the absorbed laser power.¹⁹ The mass ablation rates in spherical targets were measured using spectroscopic techniques,^{20,21} but these measurements were not able to constrain the thermal-transport models and the ablation pressure in imploding targets, in part because of the sensitivity to perturbations at the ablation surface and the lack of trajectory measurements.

This article presents measurements of the conduction-zone length and the mass ablation rate in a direct-drive implosion. The spherical target was constructed with a thin CD ablator containing a thick cryogenic DT ice layer that enabled the use of a novel technique to measure the average mass ablation rate of the CD ($7.95 \pm 0.3 \mu\text{g/ns}$) and the conduction-zone length ($110 \pm 20 \mu\text{m}$) at the time when the laser light begins to be deposited in the ice layer. These measurements coupled with the simultaneous measurements of the absorbed laser power and ablation-front trajectory fully constrain the electron thermal transport. Hydrodynamic simulations that use nonlocal thermal transport and CBET models reproduce the experimental observables, while hydrodynamic simulations that use a time-dependent flux-limited model reproduce the shell trajectory

and the absorbed laser power, but underestimate the mass ablation rate by $\sim 10\%$ and the length of the conduction zone by nearly a factor of 2. These results highlight the importance of developing multidimensional hydrodynamic codes that include CBET and nonlocal thermal-transport models for studying hydrodynamic instabilities to accurately calculate the mass ablation rate and the conduction zone length.

The experiments employed 60 ultraviolet ($\lambda_0 = 351$ nm) laser beams at the Omega Laser Facility.²² The laser beams uniformly illuminated the target and were smoothed by polarization smoothing,²³ smoothing by spectral dispersion,²⁴ and distributed phase plates²⁵ (fourth-order super-Gaussian with 95% of the energy contained within the initial target diameter). Two 100-ps-long pickets were used to set the target implosion onto a low adiabat ($\alpha = 2.8$) (Ref. 26) followed by a 2-ns pulse that drove the target to its final velocity [Fig. 141.5(a)]. The total energy of the laser was 24.4 ± 0.2 kJ, which resulted in a maximum on-target overlapped intensity of 1×10^{15} W/cm². The target had an 868- μm outer diameter with a 7.2- μm -thick CD ablator (18.6 ± 0.6 μg) containing a 62.8- μm -thick cryogenic DT ice layer (28.3 ± 0.6 μg).

The total unabsorbed laser energy was measured by five calorimeters located around the target chamber with an absolute uncertainty of 5%. The scattered-light spectra were measured at four locations by multiplexing the signal into a 1.5-m spectrometer with a high-dynamic-range streak camera. The system has a 100-ps full width at half maximum (FWHM) temporal resolution and a 0.3- \AA FWHM spectral resolution.

The recently developed self-emission x-ray imaging technique²⁸ was used to simultaneously measure the CD/DT interface and the ablation-surface trajectories [Fig. 141.5(b)]. The soft x rays emitted by the imploding target were integrated over 40 ps and imaged with an array of 20- μm -diam pinholes onto a four-strip fast x-ray framing camera (XRFC),²⁹ with a $6\times$ magnification. The absolute timing of the measurements was known to an accuracy of 30 ps and the interstrip timing was determined within 5 ps (Ref. 30).

Figure 141.5(c) shows the calculated x-ray self-emission profile after the laser has burned through the outer CD layer (black curve). The outer peak in this profile corresponds to the radius of the CD/DT interface. The flux at the detector increases with decreasing radius as a result of the increasing integration length along the line of sight of the diagnostic [orange region in Fig. 141.5(b)]. This line-integrated flux begins to decrease at the CD/DT interface because the DT x-ray emission is reduced relative to the CD emission. The flux increases between the CD/DT interface and the ablation surface [blue region of Fig. 141.5(b)] because of the radially increasing density. When the electron temperature drops below 100 eV (ablation surface), the emission of >1 -keV x rays approaches zero and the x rays emitted on the opposite side of the target from the detector are absorbed. This results in a rapid decrease in the line-integrated flux over a few microns, providing an excellent measure of the ablation surface's location.²⁸

Figure 141.6 shows the emission profiles that were azimuthally averaged over 360° and were determined from the self-

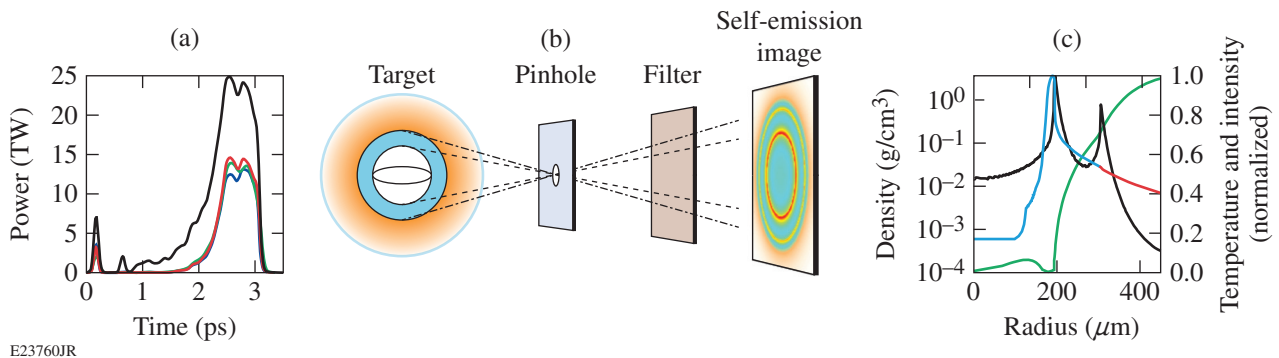


Figure 141.5

(a) The laser pulse shape (black curve) is shown along with a comparison of the measured time-resolved scattered-light power (green curve), calculated with hydrodynamic simulation using the nonlocal thermal transport and cross-beam energy transfer (CBET) models (red curve) and using the time-dependent flux-limiter model (blue curve). (b) Self-emission x-ray image calculated after the laser has burned through the outer CD layer. The image contains two rings: the inner ring corresponds to the emission at the ablation surface (dashed lines) and the outer ring corresponds to the emission at the CD/DT interface (dotted-dashed line). (c) Comparison of the density profile (the blue curve corresponds to DT and the orange curve corresponds to CD), normalized temperature profile (green curve), and normalized self-emission lineout (black curve) calculated 460 ps after the laser has burned through the outer CD layer. In (b) and (c), the x-ray self-emission was calculated by post-processing the hydrodynamic simulation with *Spect3D*.²⁷

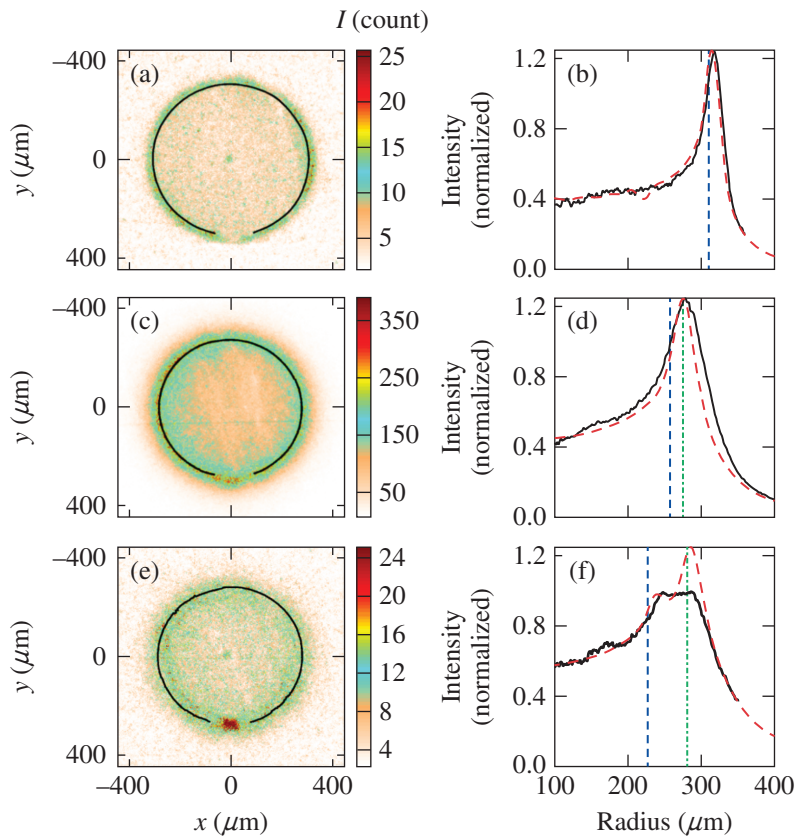


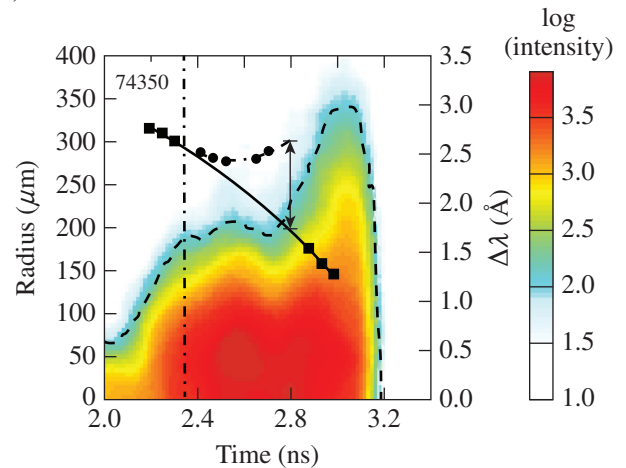
Figure 141.6

[(a),(c),(e)] Self-emission images and [(b),(d),(f)] profiles azimuthally averaged over 360° (black line) measured at [(a),(b)] $t = 2.2$ ns, [(c),(d)] $t = 2.5$ ns, and [(e),(f)] $t = 2.6$ ns. [(a),(c),(e)] The positions of the radial shifts added to the peak intensity determined in the 360° -averaged profile are plotted (black line). [(b),(d),(f)] The self-emission profiles (dashed red lines), the position of the ablation front (dashed blue line), and the position of the CD/DT interface (dashed-dotted green line) calculated with the hydrodynamic simulations using the nonlocal thermal transport and CBET models. The calculated profiles were convolved using the point-spread function of the diagnostic.^{28,31}

E23761JR

emission images. The center of each image was determined iteratively. Intensity profiles were taken along chords through the center of the image and azimuthally averaged over 20° . The radial shifts between the 360° -averaged emission profile and each 20° -averaged emission profile were determined by χ^2 analysis. A contour was defined by adding the radial shifts to the radius of the peak intensity determined from the 360° -averaged profile. A new center was calculated by comparing this contour to a circle using a χ^2 analysis. This process was repeated until the center changed by no more than $0.1 \mu\text{m}$. A standard deviation $< 3 \mu\text{m}$ was obtained in the position of each 20° -averaged emission profile relative to the 360° -averaged emission profile [black line in Figs. 141.6(a), 141.6(c), and 141.6(e)]. This resulted in a negligible spatial convolution to the 360° -averaged emission profiles (about the size of this measured standard deviation).

Figure 141.7 shows the measured CD/DT interface and ablation-front trajectories. At $t = 2.34 \pm 0.05$ ns, the CD begins to expand from the ablation surface, indicating that the initial $18.6 \pm 0.6 \mu\text{g}$ of CD has been ablated. This results in an averaged mass ablation rate of $7.95 \pm 0.3 \mu\text{g/ns}$. At this time, the mass of the shell corresponds to the difference in the initial mass of the DT layer ($28.3 \pm 0.6 \mu\text{g}$) and the DT that has been released into



E23762JR

Figure 141.7

Measured ablation front (squares) and CD/DT interface (diamond) trajectories are plotted (left axis) on top of the measured scattered-light spectrum (right axis). Third-order polynomials are fit to the ablation front (solid curve) and to the CD/DT interface (dashed curve). The CD is ablated at 2.34 ns when the CD/DT interface separates from the ablation surface (dashed-dotted line). The 5% intensity contour is used to determine the maximum wavelength shift (dashed curve). The rapid increase in wavelength shift at 2.8 ns is a result of the CD/DT interface crossing the critical-density surface. The length of the conduction zone is determined from the distance between the ablation surface and CD/DT interface at the time when the interface crosses the critical-density surface (black double arrow).

the hot spot (simulations indicate $\sim 0.4 \mu\text{g}$). The ablation front and CD/DT interface trajectories were determined following the method described in Ref. 31, where a detailed analysis of the instrument function and opacities quantify the positions of the ablation front and the material interface. The ablation front is located $3 \mu\text{m}$ inward from the inner peak [Fig. 141.6(b)]. Through most of the implosion, the CD/DT interface is best tracked by the peak [Fig. 141.6(d)], but when the intensities of the inner and outer peaks are comparable [Fig. 141.6(f)], the outer peak becomes an edge, so a robust criterion was developed to determine the position of the interface. The maximum slope averaged over $30 \mu\text{m}$ along the outer edge of the profile is determined, extended beyond the interface radius and the interface position corresponds to the point where the measured intensity deviates from the extended line by 10% (Ref. 31).

The CD burnthrough time is confirmed by the scattered-light spectra, where a flattening of the maximum shifted scatter light (Fig. 141.7) is observed at $t \sim 2.35 \pm 0.1 \text{ ns}$, indicating that the acceleration of the critical-density surface is reduced. This is a consequence of the increased length of the conduction zone that occurs when the DT begins to ablate. At this time the mass ablation rate increases because of an increase in $\langle A \rangle / \langle Z \rangle$, where $\langle A \rangle$ is the averaged atomic mass and $\langle Z \rangle$ is the averaged atomic number near the ablation surface.³²

The distance between the CD/DT interface and the ablation surface at the time when the CD/DT interface reaches the critical surface (absorption region) provides a measure of the length of the conduction zone. The unabsorbed light with the maximum red-shifted wavelength (dashed curve in Fig. 141.7) results from rays with their turning point near the critical surface. The jump in the maximum red-shifted wavelength from 1.7 \AA to 3 \AA (Fig. 141.7) observed at $t = 2.87 \text{ ns}$ (half-intensity point in the rise of the shift) corresponds to the time when the CD/DT interface reaches the turning point of the unabsorbed light. It is a result of a jump in the radial position of the critical density between the CD and the DT (the difference in $\langle A \rangle / \langle Z \rangle$, combined with the continuity of the mass flux results in a jump in the electron density). Because the turning point in DT is closer to the ablation surface than in CD, the inward velocity of the turning point is larger in DT, leading to a larger frequency shift.³² When accounting for the distance between the critical surface and this turning point (simulations show $\sim 70 \text{ ps}$), the CD/DT interface is determined to reach the critical surface at $t = 2.8 \pm 0.05 \text{ ns}$. At this time the length of the conduction zone is $110 \pm 20 \mu\text{m}$. The error bar corresponds to the simulated

variation of the distance between the ablation front and the CD/DT interface over the 50-ps uncertainty in the measurement.

Figure 141.8(a) shows an excellent agreement between the measured and the simulated trajectories when the *LILAC*³³ simulation uses nonlocal thermal transport and CBET models. This is consistent with the good agreement observed in the self-emission profiles (Fig. 141.6). The small differences in the profiles observed in Figs. 141.6(d) and 141.6(f) are likely a

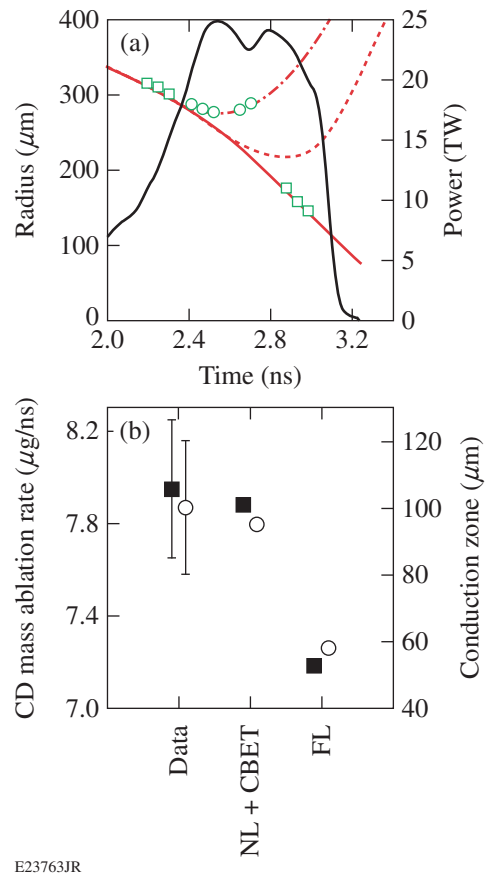


Figure 141.8

(a) Comparison of the measured ablation front (squares) and CD/DT interface (circles) trajectories with ablation front (solid red curve) and the CD/DT interface (dashed-dotted red curve) calculated using a simulation that includes nonlocal thermal transport and cross-beam energy transfer models (NL + CBET) and the CD/DT interface trajectory calculated using a simulation with a time-dependent, flux-limited (FL) thermal-transport model (dashed red curve). The flux limiter was adapted to have the ablation-front radius match the measured ablation front at each time. The laser pulse (black curve) corresponds to the right axis. (b) Comparison of the averaged mass ablation rate of the CD (solid squares) and the size of the conduction zone (open circles) measured at $t = 2.8 \text{ ns}$ with simulations that use nonlocal thermal transport and CBET models and a time-dependent flux-limiter model.

result of perturbation growth at the CD/DT interface, but this has a negligible effect on measuring the interface trajectories.³¹ Excellent agreement between the measured and simulated CD burnthrough times indicates that the averaged mass ablation rate of the CD is well modeled. These measurements of the averaged mass ablation rate, the shell trajectory, and the laser absorption significantly constrain the hydrodynamic modeling, as evident by the simulation performed using a Spitzer–Härm heat-transport model [Fig. 141.8(a)]. In this simulation, the flux limiter was varied at each time step to match the measured shell trajectory. With this model, the laser burns through the outer CD layer 250 ps later than in the measurements, indicating that the averaged mass ablation rate is underestimated by 10% [Fig. 141.8(b)]. This results in a more-massive shell and an overestimate of the shell’s kinetic energy by 10%. At maximum compression, the mass of the shell calculated by the two models differs by 26%. These results show that time-dependent flux-limiter simulations cannot reproduce simultaneously the shell mass and trajectory.

The measured and calculated sizes of the conduction zone at $t = 2.8$ ns are compared in Fig. 141.8(b). Excellent agreement is obtained when the simulation uses nonlocal thermal transport and CBET models. When using a time-dependent flux limiter, the lower thermal flux reduces the conduction zone to 58 μm , which corresponds to nearly a factor of 2 smaller than measured.

In summary, the size of the conduction zone, the mass ablation rate, the shell trajectory, and the absorbed laser power were measured in direct-drive cryogenic experiments. These measurements quantify the electron thermal transport from the laser-absorption region to the ablation front. Hydrodynamic simulations that include nonlocal thermal transport and CBET models accurately reproduce these experimental observables. When a time-dependent flux limiter was used to match the measured shell trajectory, the laser absorption was well reproduced, but the mass ablation rate was underestimated by $\sim 10\%$ and the conduction-zone length by nearly a factor of 2. These results highlight the importance of developing multidimensional hydrodynamic codes that include CBET and nonlocal thermal-transport models to accurately determine the energy flow between the laser-absorption region and the ablation surface, particularly when studying effects that depend on the mass ablation rate. For example, when studying the effects of the RT instability on target performance using hydrodynamic simulations that use Spitzer–Härm thermal transport with a

time-dependent flux limiter adjusted to match the shell trajectory, the mass ablation rate is underestimated, leading to a shorter conduction zone. The shorter conduction zone produces a higher level of laser imprint, which seeds the RT instability, while the lower mass ablation rate underestimates the reduction in the perturbation growth at the ablation surface. Both of these errors overestimate the effects of the RT instability on target performance.

ACKNOWLEDGMENT

This material is based upon work supported by the Department of Energy National Nuclear Security Administration under Award Number DE-NA0001944, the University of Rochester, and the New York State Energy Research and Development Authority. The support of DOE does not constitute an endorsement by DOE of the views expressed in this article.

REFERENCES

1. R. P. Drake, *High-Energy-Density Physics: Fundamentals, Inertial Fusion, and Experimental Astrophysics, Shock Wave and High Pressure Phenomena* (Springer, Berlin, 2006).
2. J. Nuckolls *et al.*, *Nature* **239**, 139 (1972).
3. S. X. Hu, V. N. Goncharov, P. B. Radha, J. A. Marozas, S. Skupsky, T. R. Boehly, T. C. Sangster, D. D. Meyerhofer, and R. L. McCrory, *Phys. Plasmas* **17**, 102706 (2010).
4. M. H. Emery *et al.*, *Phys. Rev. Lett.* **48**, 253 (1982).
5. S. E. Bodner, *Phys. Rev. Lett.* **33**, 761 (1974).
6. R. Betti, V. N. Goncharov, R. L. McCrory, and C. P. Verdon, *Phys. Plasmas* **5**, 1446 (1998).
7. R. C. Malone, R. L. McCrory, and R. L. Morse, *Phys. Rev. Lett.* **34**, 721 (1975).
8. R. L. McCrory, J. M. Soures, C. P. Verdon, P. Audebert, D. Bradley, J. Delettrez, R. Hutchison, S. D. Jacobs, P. Jaanimagi, R. Keck, H. Kim, T. Kessler, J. Knauer, R. Kremens, S. Letzring, F. Marshall, P. McKenty, M. C. Richardson, A. Simon, R. Short, S. Skupsky, and B. Yaakobi, in *High Intensity Laser-Matter Interactions*, edited by E. M. Campbell and H. Baldis (SPIE, Bellingham, WA, 1988), Vol. 913, pp. 40–58.
9. A. Sunahara, J. A. Delettrez, C. Stoeckl, R. W. Short, and S. Skupsky, *Phys. Rev. Lett.* **91**, 095003 (2003).
10. S. X. Hu, V. Smalyuk, V. N. Goncharov, S. Skupsky, T. C. Sangster, D. D. Meyerhofer, and D. Shvarts, *Phys. Rev. Lett.* **101**, 055002 (2008).
11. I. V. Igumenshchev, V. N. Goncharov, W. T. Shmayda, D. R. Harding, T. C. Sangster, and D. D. Meyerhofer, *Phys. Plasmas* **20**, 082703 (2013).
12. J. F. Luciani, P. Mora, and J. Virmont, *Phys. Rev. Lett.* **51**, 1664 (1983).
13. E. M. Epperlein and R. W. Short, *Phys. Fluids B* **3**, 3092 (1991).

14. G. P. Schurtz, Ph. D. Nicolaï, and M. Busquet, *Phys. Plasmas* **7**, 4238 (2000).
15. V. N. Goncharov, O. V. Gotchev, E. Vianello, T. R. Boehly, J. P. Knauer, P. W. McKenty, P. B. Radha, S. P. Regan, T. C. Sangster, S. Skupsky, V. A. Smalyuk, R. Betti, R. L. McCrory, D. D. Meyerhofer, and C. Cherfils-Clérouin, *Phys. Plasmas* **13**, 012702 (2006).
16. G. Gregori, S. H. Glenzer, J. Knight, C. Niemann, D. Price, D. H. Froula, M. J. Edwards, R. P. J. Town, A. Brantov, W. Rozmus, and V. Yu. Bychenkov, *Phys. Rev. Lett.* **92**, 205006 (2004).
17. O. Gotchev, V. N. Goncharov, J. P. Knauer, T. R. Boehly, T. J. B. Collins, R. Epstein, P. A. Jaanimagi, and D. D. Meyerhofer, *Phys. Rev. Lett.* **96**, 115005 (2006).
18. I. V. Igumenshchev, D. H. Edgell, V. N. Goncharov, J. A. Delettrez, A. V. Maximov, J. F. Myatt, W. Seka, A. Shvydky, S. Skupsky, and C. Stoeckl, *Phys. Plasmas* **17**, 122708 (2010).
19. D. H. Froula, I. V. Igumenshchev, D. T. Michel, D. H. Edgell, R. Follett, V. Yu. Glebov, V. N. Goncharov, J. Kwiatkowski, F. J. Marshall, P. B. Radha, W. Seka, C. Sorce, S. Staginitto, C. Stoeckl, and T. C. Sangster, *Phys. Rev. Lett.* **108**, 125003 (2012).
20. D. K. Bradley, J. A. Delettrez, and C. P. Verdon, *Phys. Rev. Lett.* **68**, 2774 (1992).
21. S. P. Regan, R. Epstein, V. N. Goncharov, I. V. Igumenshchev, D. Li, P. B. Radha, H. Sawada, W. Seka, T. R. Boehly, J. A. Delettrez, O. V. Gotchev, J. P. Knauer, J. A. Marozas, F. J. Marshall, R. L. McCrory, P. W. McKenty, D. D. Meyerhofer, T. C. Sangster, D. Shvarts, S. Skupsky, V. A. Smalyuk, B. Yaakobi, and R. C. Mancini, *Phys. Plasmas* **14**, 056305 (2007).
22. T. R. Boehly, D. L. Brown, R. S. Craxton, R. L. Keck, J. P. Knauer, J. H. Kelly, T. J. Kessler, S. A. Kumpan, S. J. Loucks, S. A. Letzring, F. J. Marshall, R. L. McCrory, S. F. B. Morse, W. Seka, J. M. Soures, and C. P. Verdon, *Opt. Commun.* **133**, 495 (1997).
23. T. R. Boehly, V. A. Smalyuk, D. D. Meyerhofer, J. P. Knauer, D. K. Bradley, R. S. Craxton, M. J. Guardalben, S. Skupsky, and T. J. Kessler, *J. Appl. Phys.* **85**, 3444 (1999).
24. S. Skupsky, R. W. Short, T. Kessler, R. S. Craxton, S. Letzring, and J. M. Soures, *J. Appl. Phys.* **66**, 3456 (1989).
25. T. J. Kessler, Y. Lin, J. J. Armstrong, and B. Velazquez, in *Laser Coherence Control: Technology and Applications*, edited by H. T. Powell and T. J. Kessler (SPIE, Bellingham, WA, 1993), Vol. 1870, pp. 95–104.
26. V. N. Goncharov, T. C. Sangster, T. R. Boehly, S. X. Hu, I. V. Igumenshchev, F. J. Marshall, R. L. McCrory, D. D. Meyerhofer, P. B. Radha, W. Seka, S. Skupsky, C. Stoeckl, D. T. Casey, J. A. Frenje, and R. D. Petrasso, *Phys. Rev. Lett.* **104**, 165001 (2010).
27. J. J. MacFarlane *et al.*, *High Energy Density Phys.* **3**, 181 (2007).
28. D. T. Michel, C. Sorce, R. Epstein, N. Whiting, I. V. Igumenshchev, R. Jungquist, and D. H. Froula, *Rev. Sci. Instrum.* **83**, 10E530 (2012).
29. D. K. Bradley, P. M. Bell, J. D. Kilkenny, R. Hanks, O. Landen, P. A. Jaanimagi, P. W. McKenty, and C. P. Verdon, *Rev. Sci. Instrum.* **63**, 4813 (1992).
30. D. T. Michel, V. N. Goncharov, I. V. Igumenshchev, R. Epstein, and D. H. Froula, *Phys. Rev. Lett.* **111**, 245005 (2013).
31. A. K. Davis, D. T. Michel, S. X. Hu, R. S. Craxton, R. Epstein, V. N. Goncharov, I. V. Igumenshchev, T. C. Sangster, and D. H. Froula, *Rev. Sci. Instrum.* **85**, 11D616 (2014).
32. V. N. Goncharov, T. C. Sangster, R. Betti, T. R. Boehly, M. J. Bonino, T. J. B. Collins, R. S. Craxton, J. A. Delettrez, D. H. Edgell, R. Epstein, R. K. Follet, C. J. Forrest, D. H. Froula, V. Yu. Glebov, D. R. Harding, R. J. Henchen, S. X. Hu, I. V. Igumenshchev, R. Janezic, J. H. Kelly, T. J. Kessler, T. Z. Kosc, S. J. Loucks, J. A. Marozas, F. J. Marshall, A. V. Maximov, R. L. McCrory, P. W. McKenty, D. D. Meyerhofer, D. T. Michel, J. F. Myatt, R. Nora, P. B. Radha, S. P. Regan, W. Seka, W. T. Shmayda, R. W. Short, A. Shvydky, S. Skupsky, C. Stoeckl, B. Yaakobi, J. A. Frenje, M. Gatu-Johnson, R. D. Petrasso, and D. T. Casey, *Phys. Plasmas* **21**, 056315 (2014).
33. J. Delettrez, *Can. J. Phys.* **64**, 932 (1986).